Electronic Supplementary Information

Augmented photoelectrochemical water reduction: influence of copper vacancies and hole-transport layer on $CuBi_2O_4$ photocathode

Madhusudana Gopannagari,[a] D. Amaranatha Reddy,*[b], Da Hye Hong,[a] K. Arun Joshi Reddy,[a] D. Praveen Kumar,[a] Hyun S. Ahn,[a] and Tae Kyu Kim*[a]

[a]*Department of Chemistry, Yonsei University, Seoul 03722, Republic of Korea*

[b]*Department of Science, Indian Institute of Information Technology Design and Manufacturing, Kurnool, Andhra Pradesh 518007, India*

*Corresponding Authors. Emails: tkkim@yonsei.ac.kr (T.K.K.) and drreddy@iiitk.ac.in (D.A.R.)

→ Number of figures: 31

→ Number of tables: 8

→ Number of references: 20

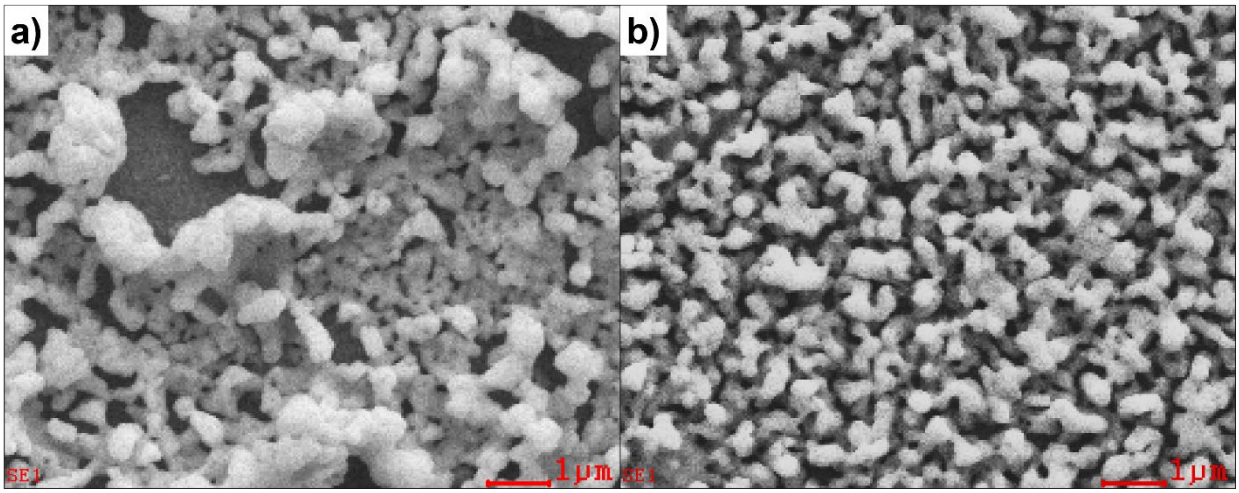

Figure S1. Top-view SEM images showing before heating process of (a) the unevenly distributed Cu/Bi film by direct electrodeposition and (b) evenly distributed Cu/Bi film by pulsed electrodeposition.

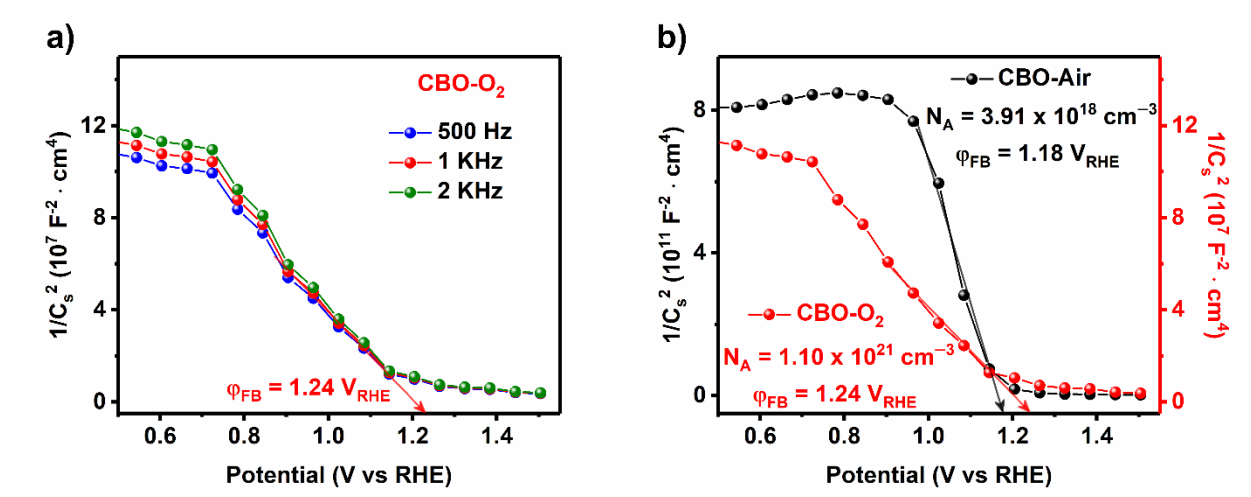

Figure S2. Mott-Schottky measurements. a) CBO-O_2 thin film performed at 0.5 kHz, 1 kHz and 2kHz. b) Comparison between pure O_2 heating and conventional furnace heating CBO thin-films without HTLs measured at 1 kHz.

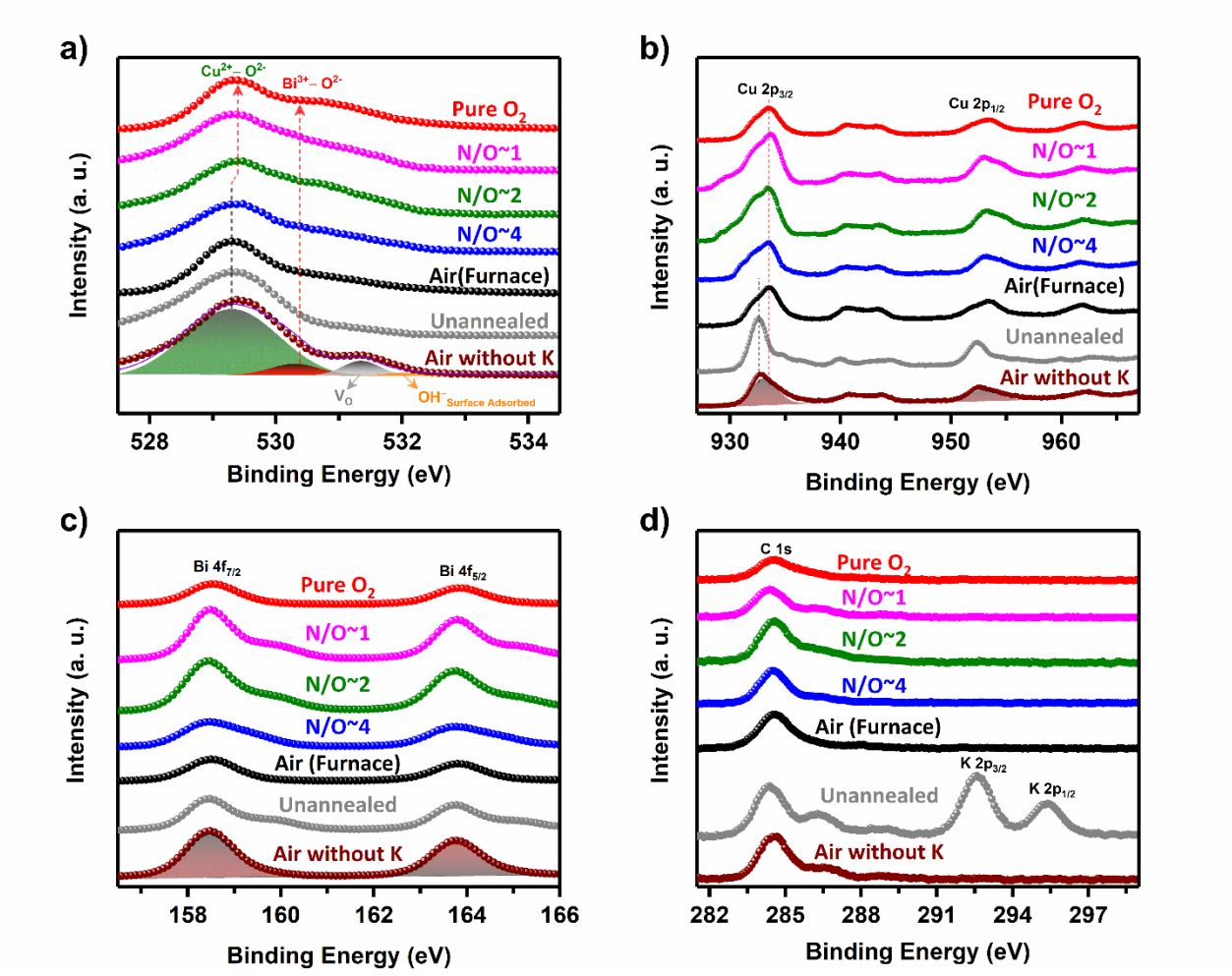

Figure S3. XPS data collected for the prepared CBO films. a) O 1s showing lattice oxygen bound to Cu and Bi, O-vacant sites (V_O) and surface adsorbed OH^-. b) Cu 2p with strong satellite peaks corresponding to Cu(II) oxidation state except in unannealed (Cu(I) oxidation was observed). c) Bi 4f, and d) C 1s, K 2p (unannealed sample only).

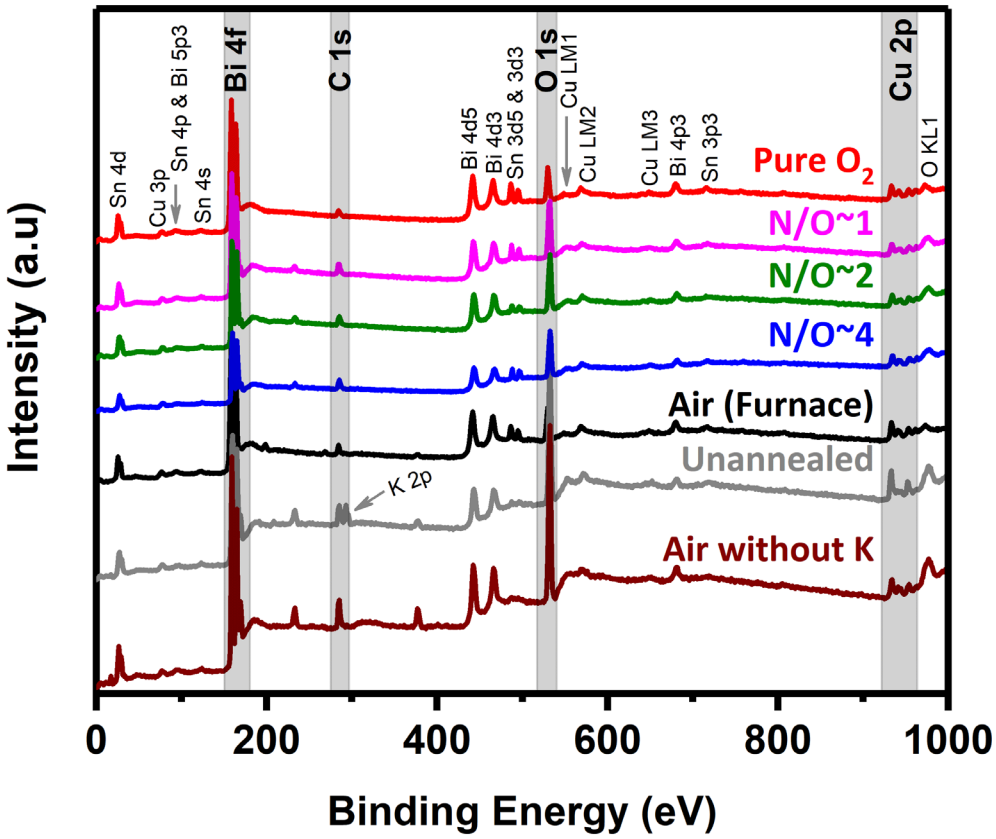

Figure S4. XPS survey spectrum for prepared CBO electrodes.

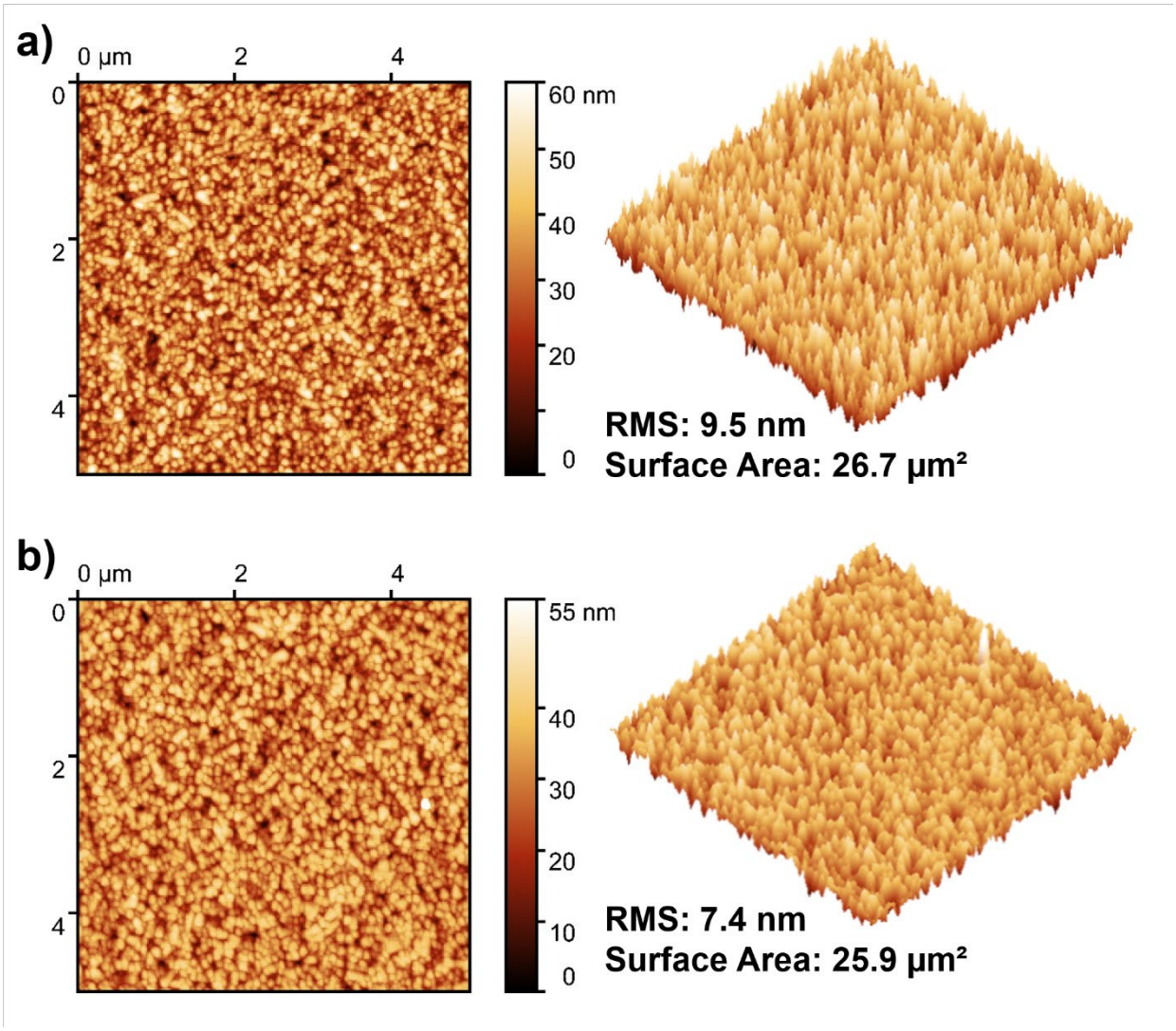

Figure S5. AFM height ($5 \times 5\ \mu m$) and 3D-AFM images of a) NiO_X and b) Fe:NiO_X HTLs on FTO substrates.

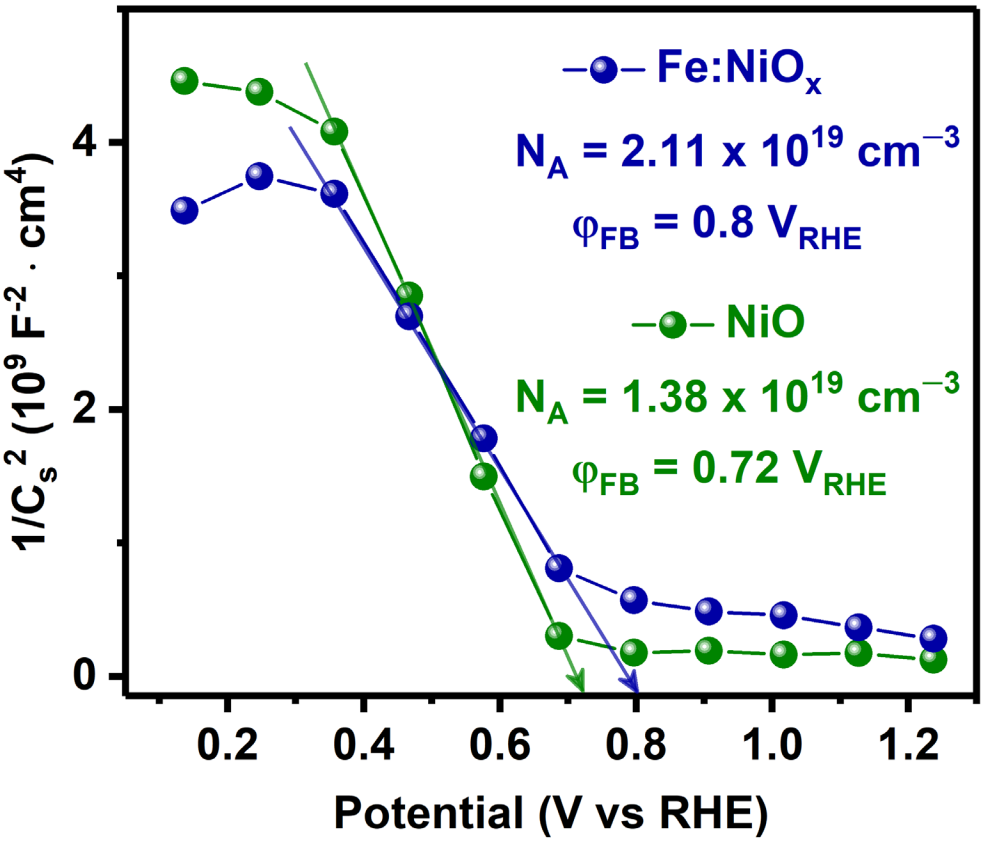

Figure S6. Mott-Schottky curves for hole-transport layer thin-films showing flat-band potentials and acceptor density.

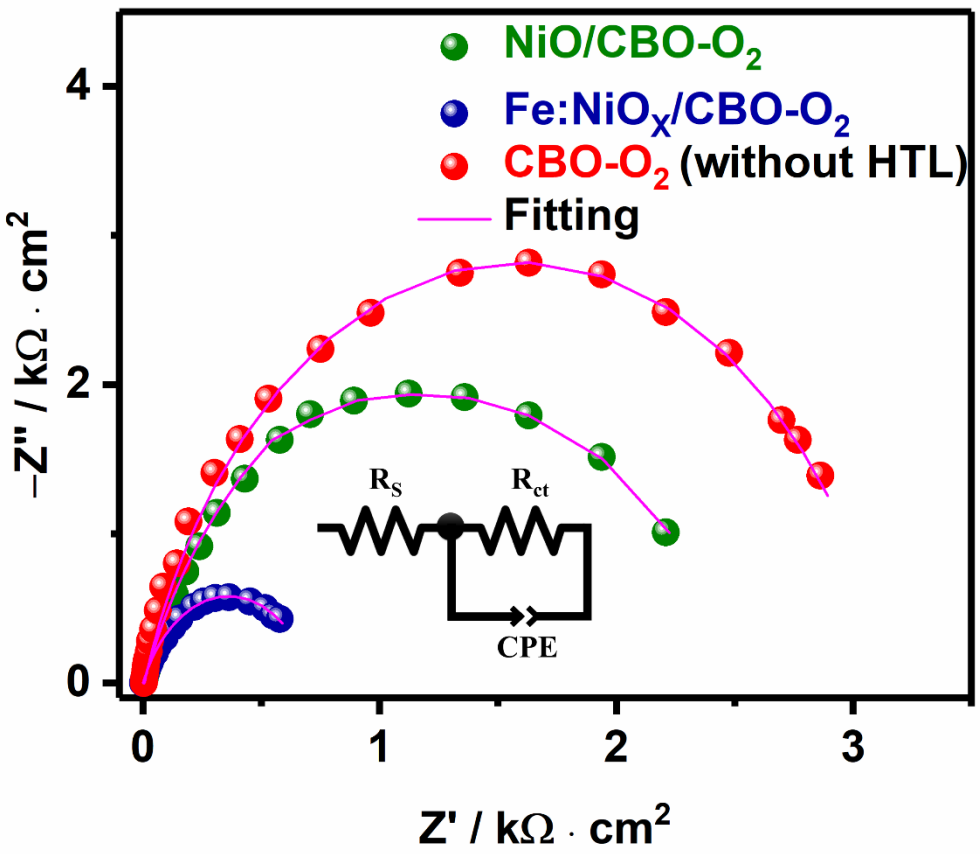

Figure S7. Electrochemical impedance spectroscopy measurements for CBO-O_2 photocathode, showing the comparison between bare NiO and Fe-doped NiO_X HTLs introduction.

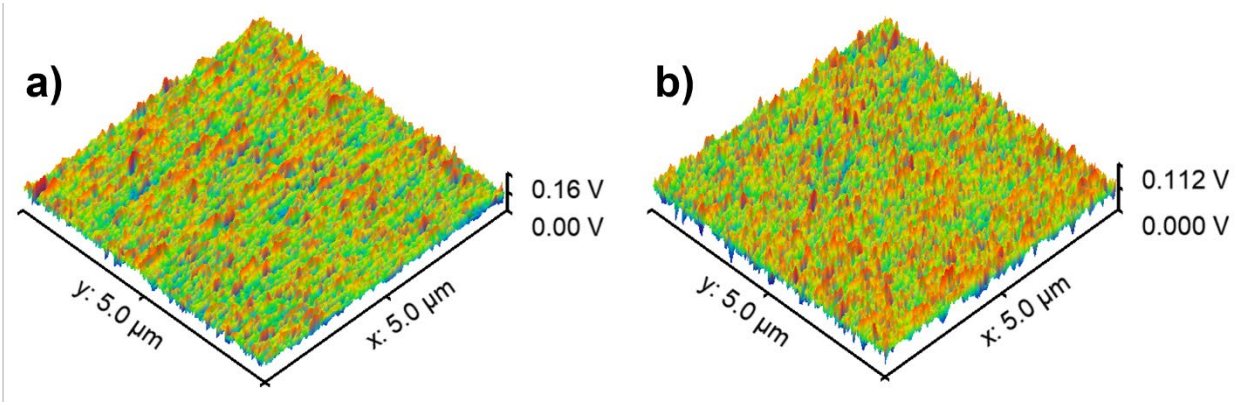

Figure S8. SKPM measurements of a) NiO_X and b) Fe:NiO_X HTLs on the FTO substrate.

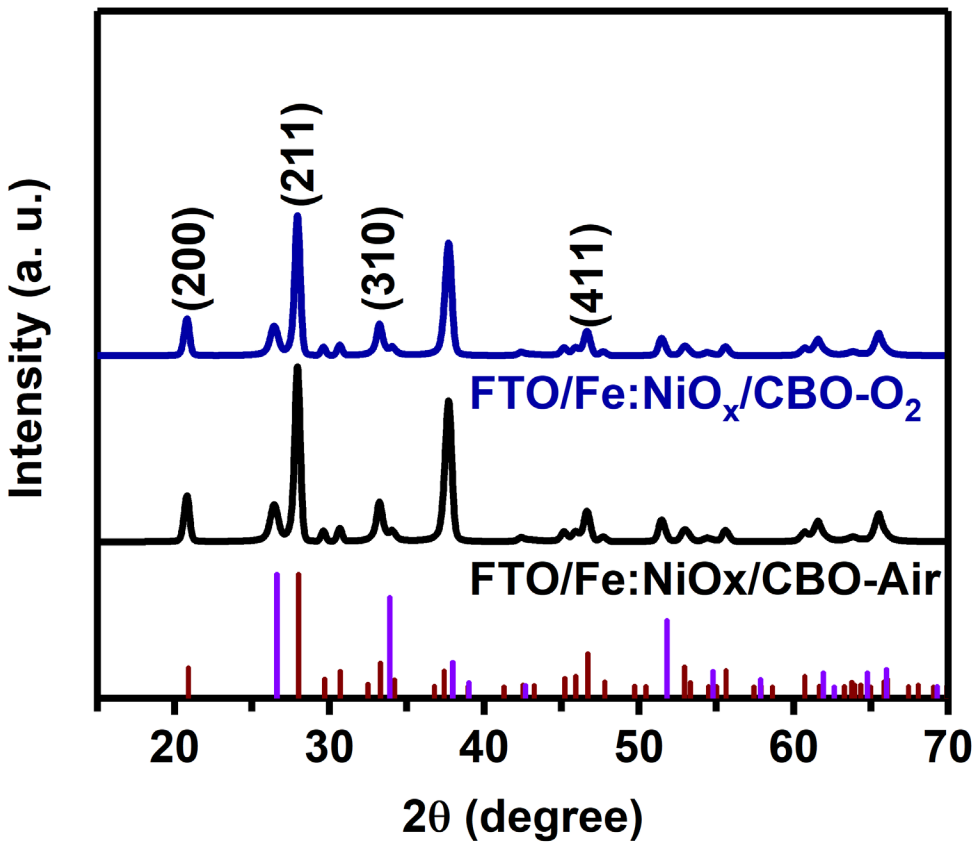

Figure S9. XRD patterns of CBO-Air and CBO-O_2 photocathodes deposited on Fe-doped NiO_X HTL.

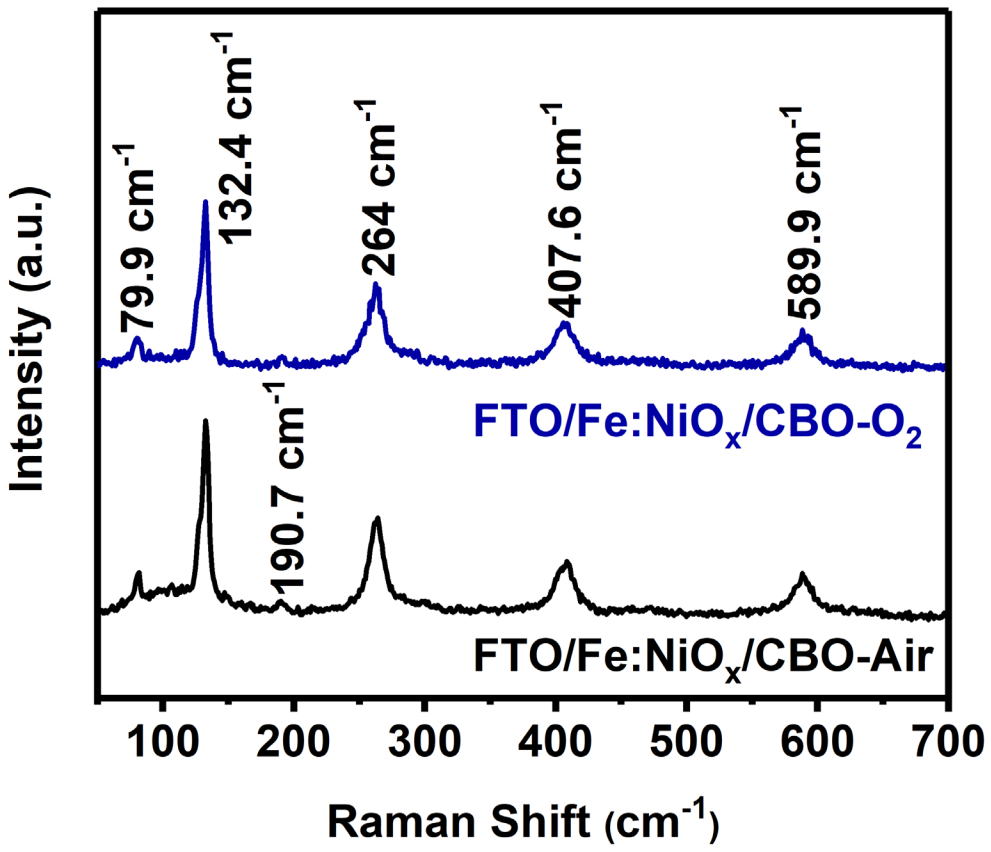

Figure S10. Raman spectra for CBO-Air and CBO-O_2 photocathodes deposited on Fe-doped NiO_X HTL.

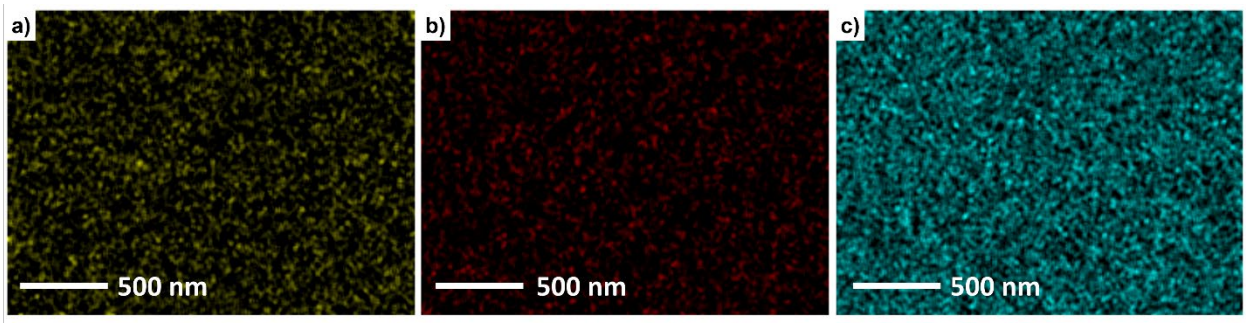

Figure S11. EDS mapping images of Fe:NiO_X-HTL deposited on FTO, showing the elemental distributions of (a) Ni, (b) Fe, and (c) O.

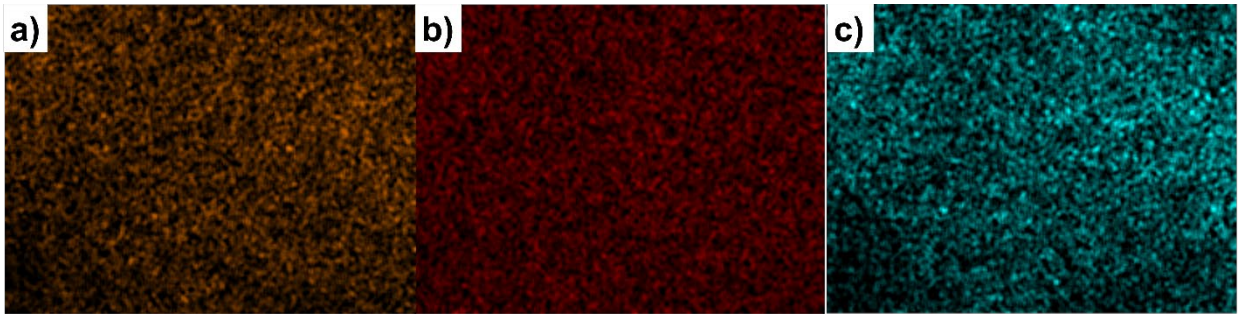

Figure S12. EDS mapping images of CBO-Air, showing the elemental distributions of (a) Cu, (b) Bi, and (c) O.

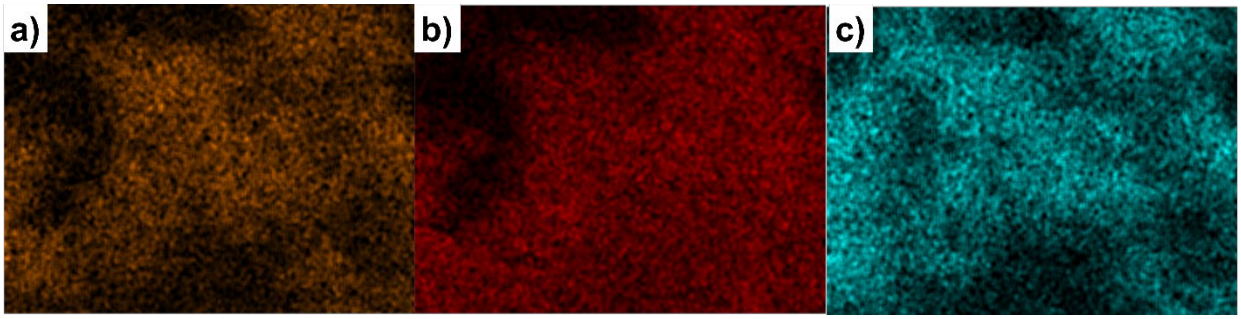

Figure S13. EDS mapping images of CBO-O_2, showing the elemental distributions of (a) Cu, (b) Bi, and (c) O.

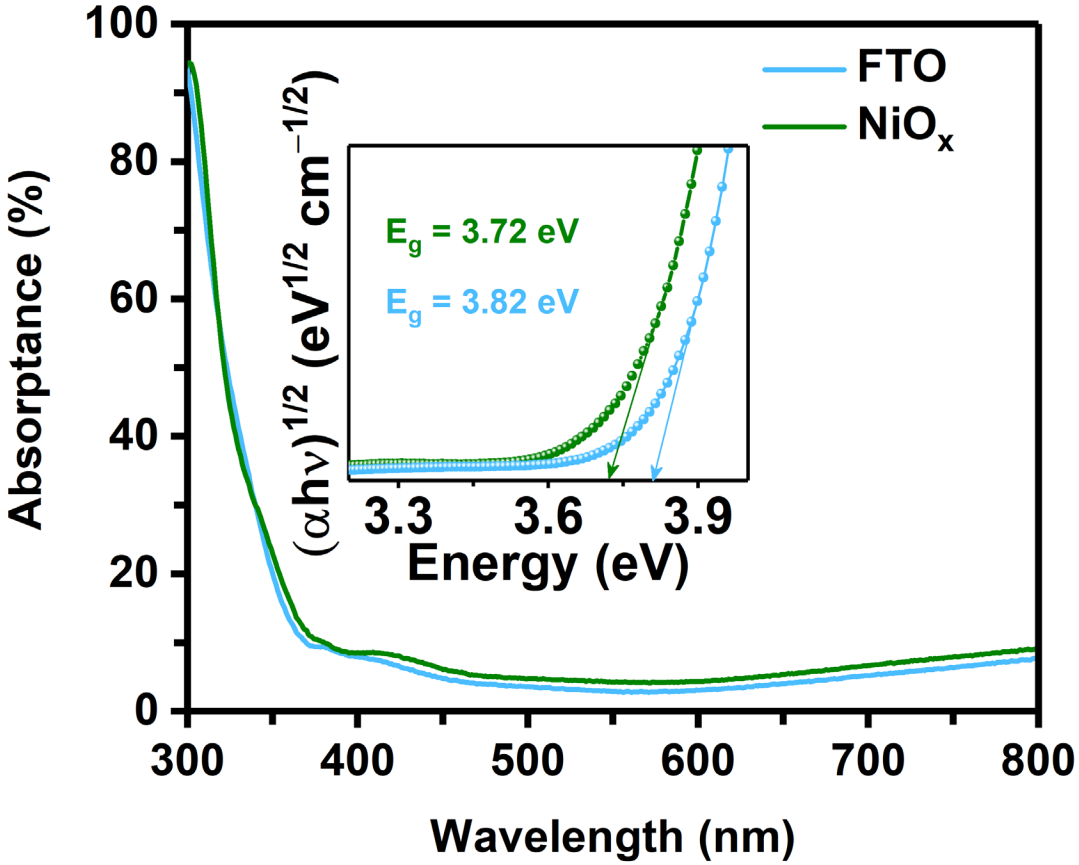

Figure S14. Absorptance of a bare FTO substrate and pristine NiO_X; comparison is shown as a reference.

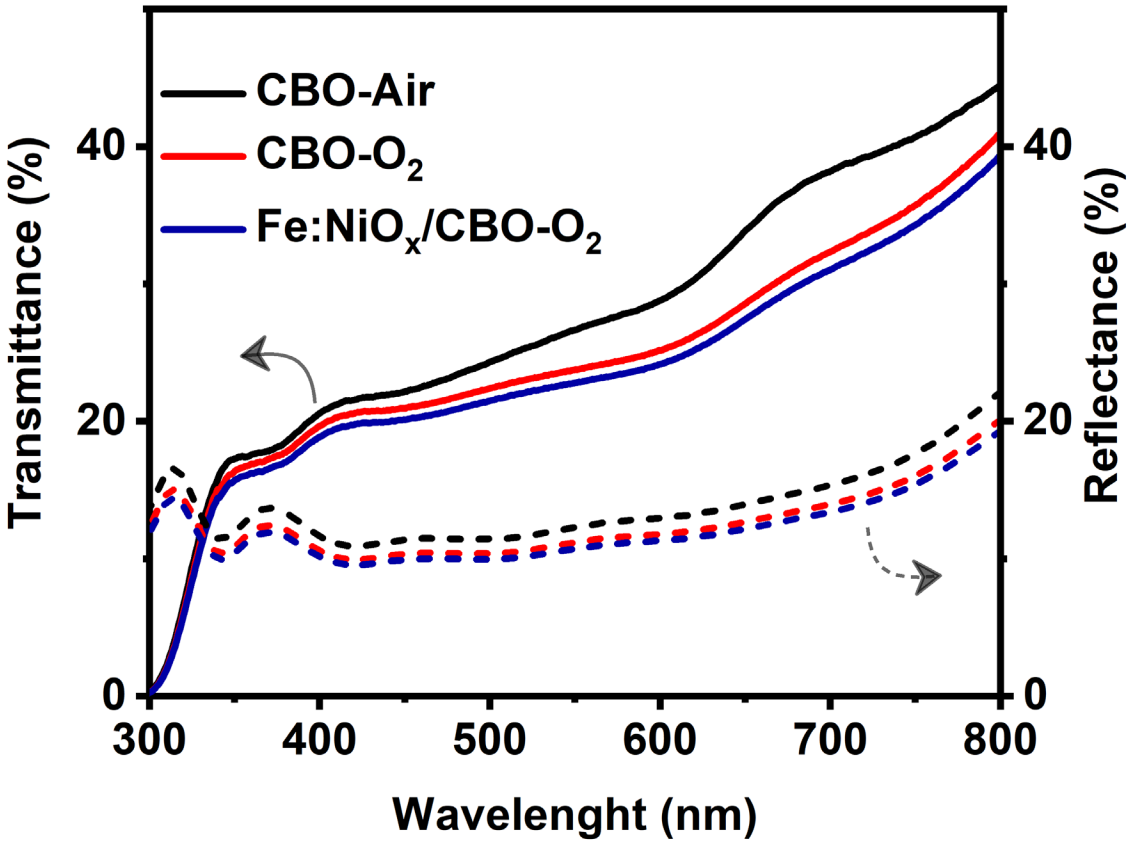

Figure S15. Transmittance and reflectance of prepared CBO photoelectrodes, compared with Fe-NiO_X/CBO-O_2 photoelectrode.

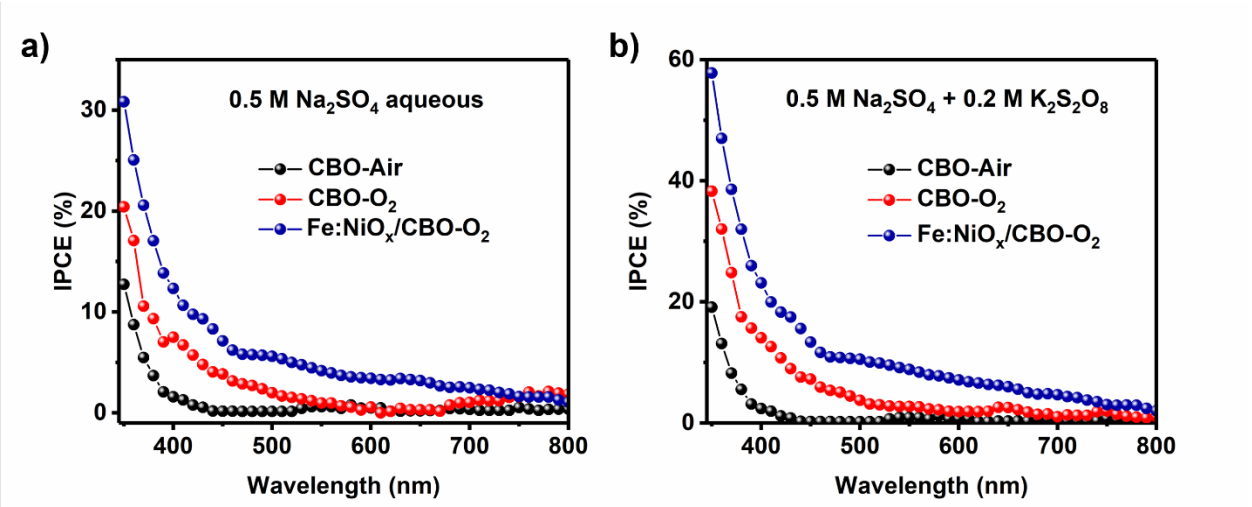

Figure S16. Incident photon-to-current efficiency (IPCE) measurements of CBO-Air, CBO-O_2 and Fe:NiO_X/CBO-O_2 photocathodes in a) 0.5 M Na_2SO_4 aqueous and b) in the presence of $K_2S_2O_8$ in the electrolyte as an electron scavenger.

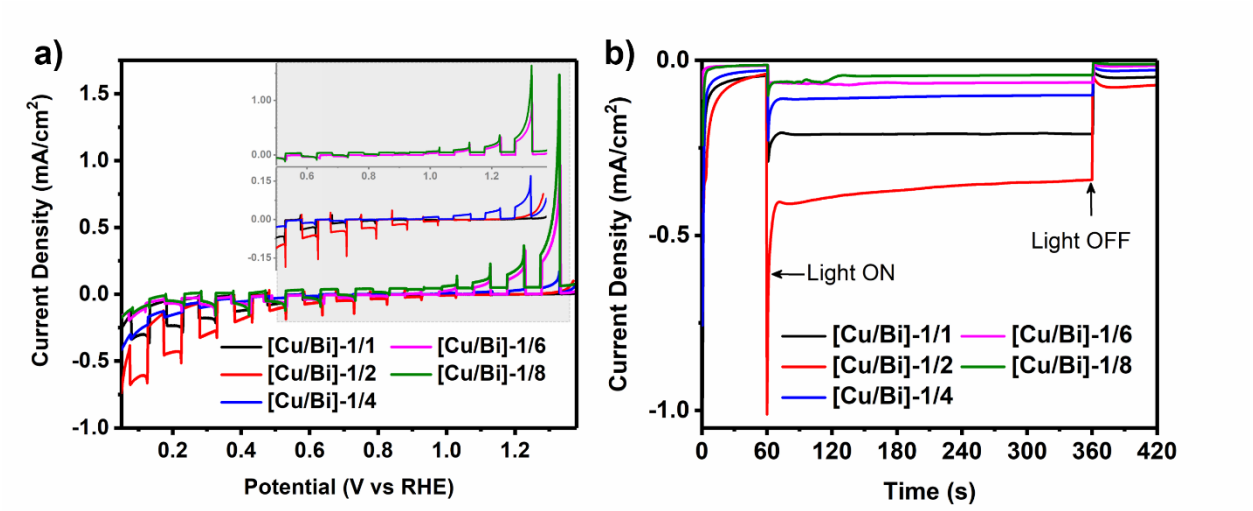

Figure S17. Cu:Bi molar ratio of FTO/CBO-Air photoelectrodes. a) Chopped LSV profile and b) photocurrent density vs. time profile at 0.2 V_{RHE} applied constant potential under dark and light conditions. Inset in a) shows the conventional furnace heating CBO electrodes with lowering the Cu-to-Bi ratio content, which leads to an increase in anodic photocurrent at the water oxidation potential for [Cu:Bi]-1/4 (blue), [Cu:Bi]-1/6 (pink) and [Cu:Bi]-1/8 (green) photocathodes.

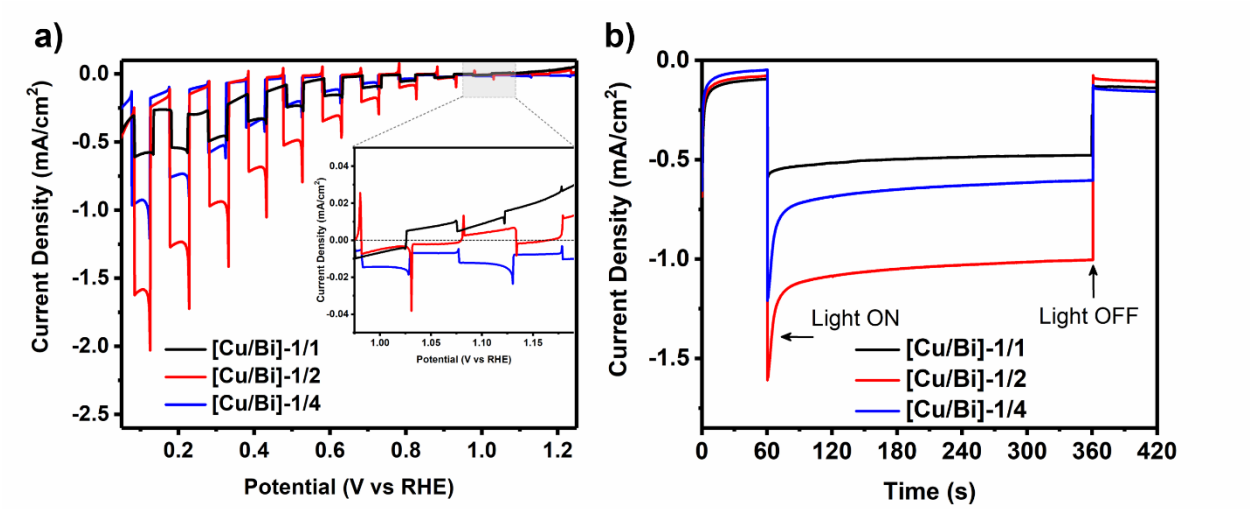

Figure S18. Cu:Bi molar ratio of FTO/CBO-O_2 photoelectrodes. a) Chopped LSV profile and b) photocurrent density vs. time profile at 0.2 V_{RHE} constant potentials applied under dark and light conditions. Inset a) shows the onset potentials.

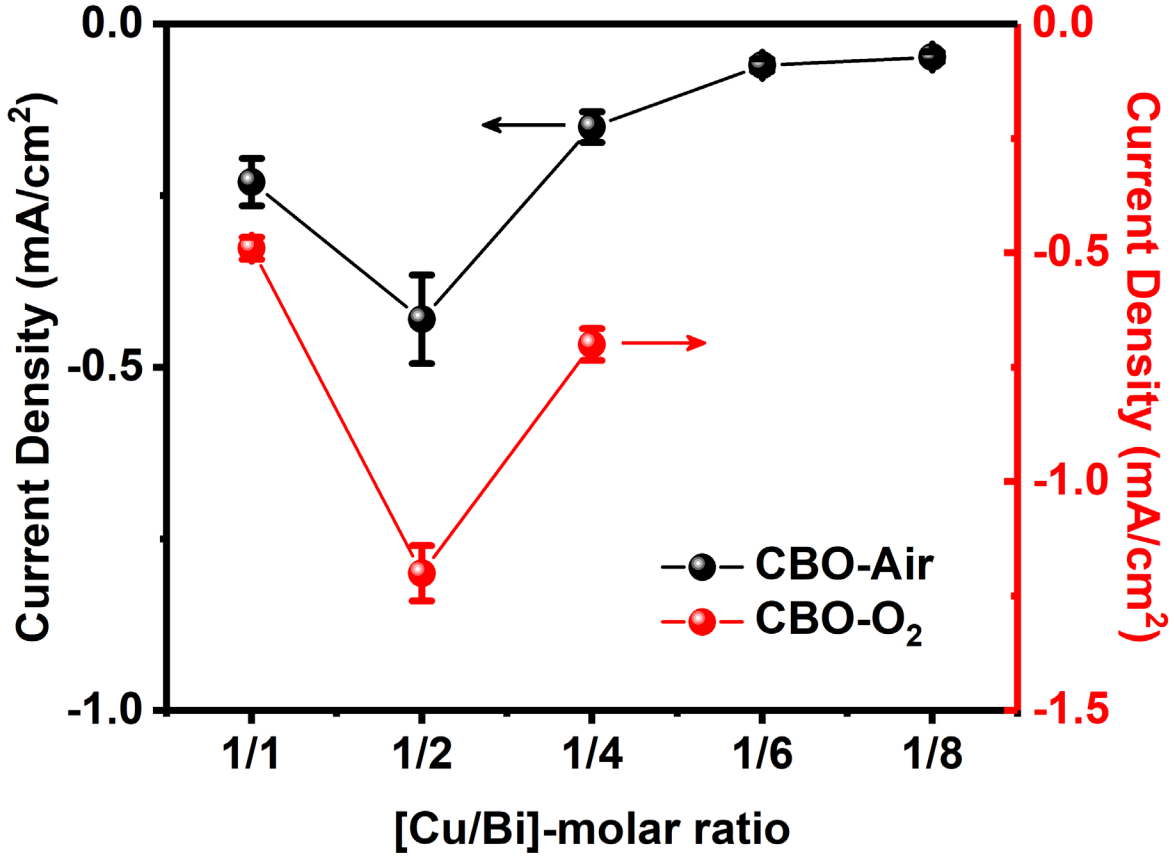

Figure S19. Photocurrent density at 0.2 V_{RHE} applied potential vs. Cu-to-Bi molar ratio of FTO/CBO-O_2 and FTO/CBO-Air photoelectrodes.

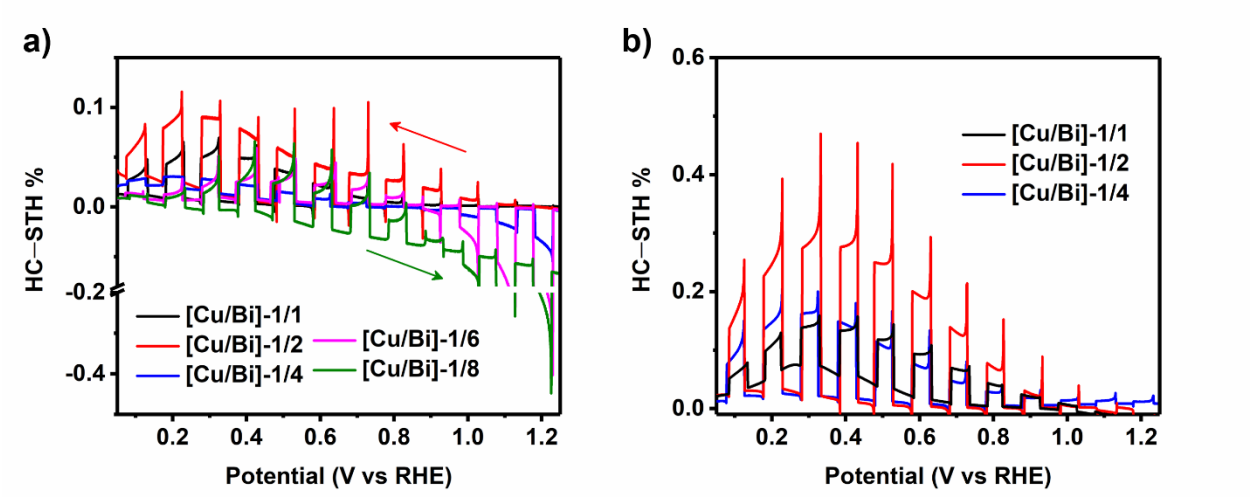

Figure S20. Comparison of HC–STH efficiency calculated from chopped LSV measurements for Cu-to-Bi molar ratio deposition on FTO substrate, a) Air and b) pure O_2 heat-treatment.

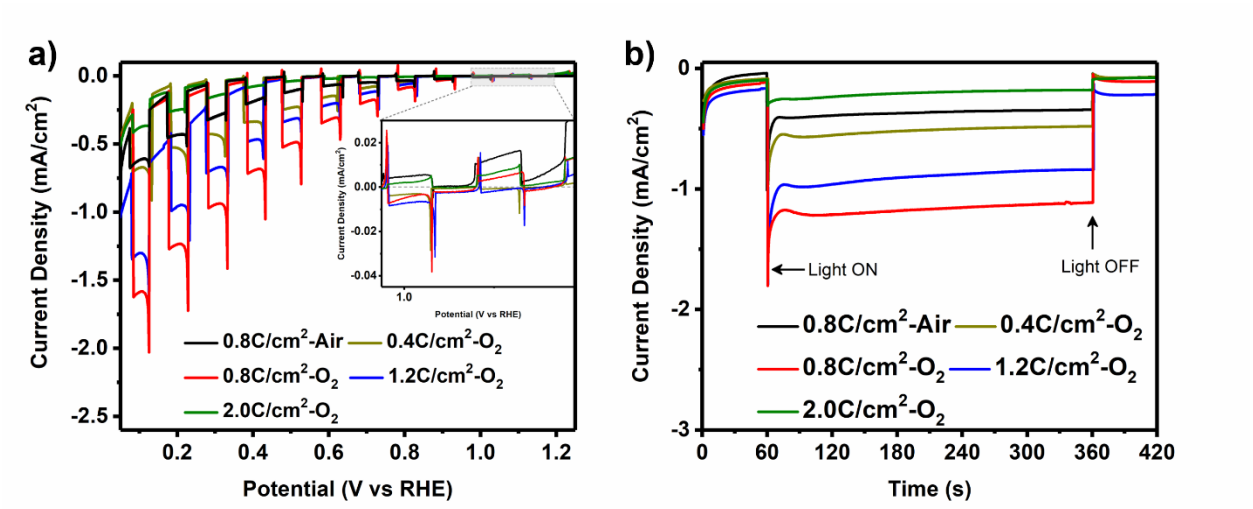

Figure S21. CBO-O_2 electrode pulsed electrodeposition charge limit: a) chopped LSV and b) transient photocurrent densities at 0.2 V_{RHE} applied potential under dark and light condition. For comparison CBO-Air electrode prepared with 0.8 C/cm^2 is included. Inset (a) shows the recorded onset potentials.

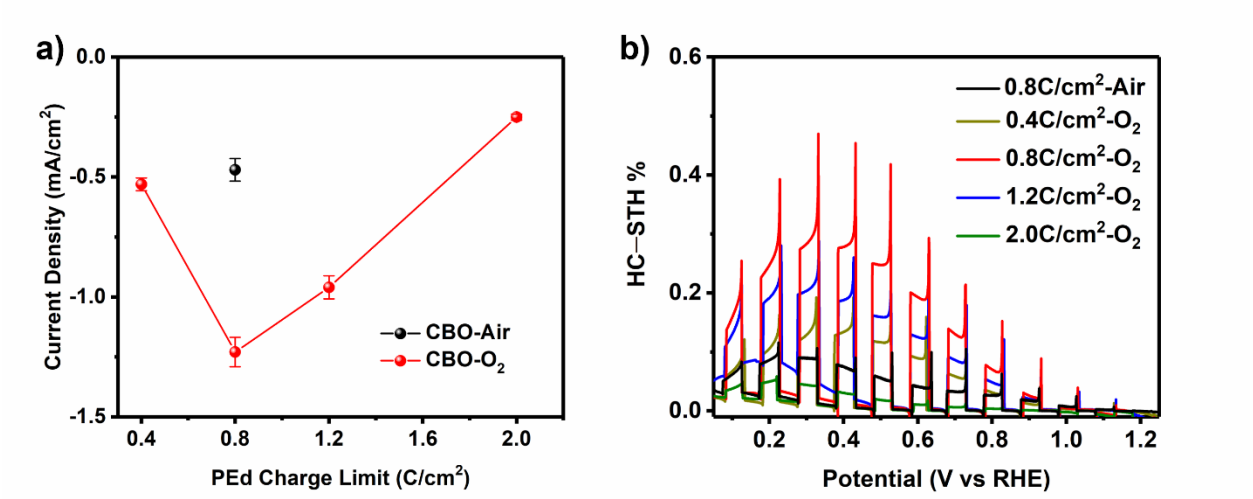

Figure S22. a) PEd charge limit vs. photocurrent density at 0.2 V_{RHE}. b) HC–STH efficiency with respect to applied potential profiles of CBO-O_2 photocathodes and comparison with CBO-Air (C-limit 0.8 C/cm^2) photocathode.

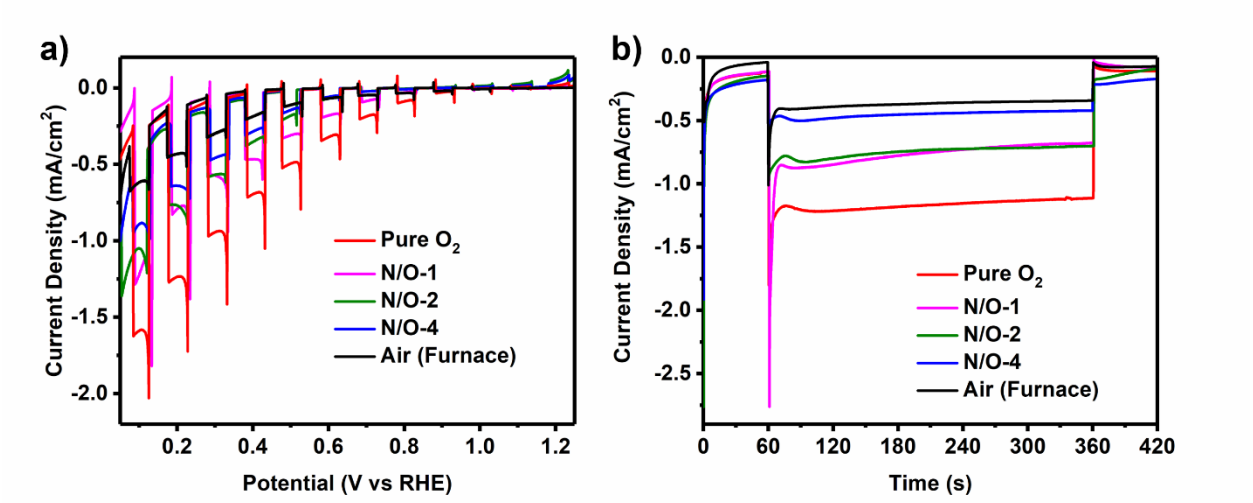

Figure S23. Different carrier gas heat-treated CBO electrodes: a) chopped LSV curves and b) transient photocurrent densities at 0.2 V_{RHE} applied potential under dark and light condition. Comparison with conventional furnace heating CBO-Air electrode is displayed, showing the parallel performance with N/O–4 electrode, which is considered as air environment in the tube furnace.

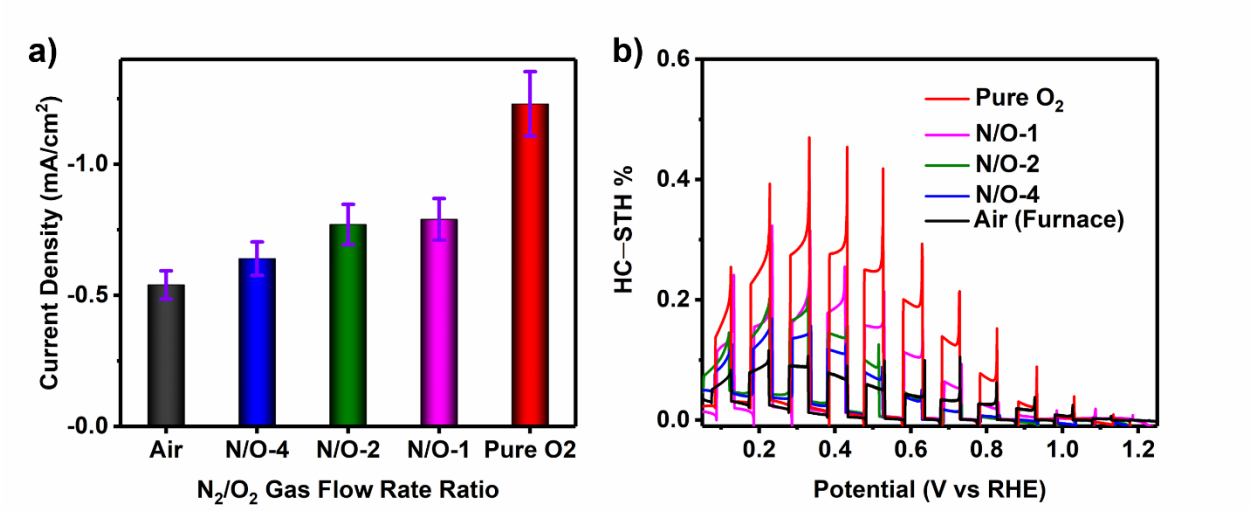

Figure S24. a) Photocurrent densities comparison at 0.2 V_{RHE} applied potential of different carrier gas heat-treated CBO electrodes. b) Respective HC–STH efficiency calculation from the LSV curves. Comparison CBO-Air photocathode is included.

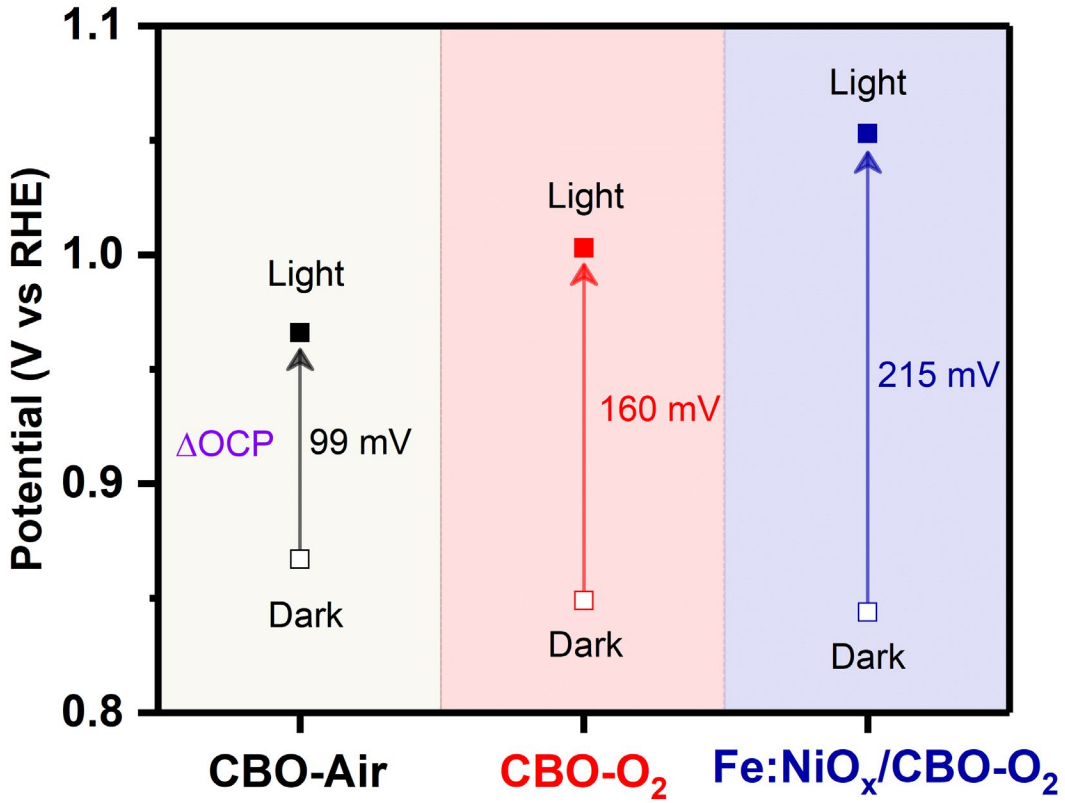

Figure S25. The significant difference observed between the OCP measured photovoltages (ΔOCP) generated by CBO-Air and CBO-O_2 photoelectrode with/without Fe:NiO_X hole transport layer.

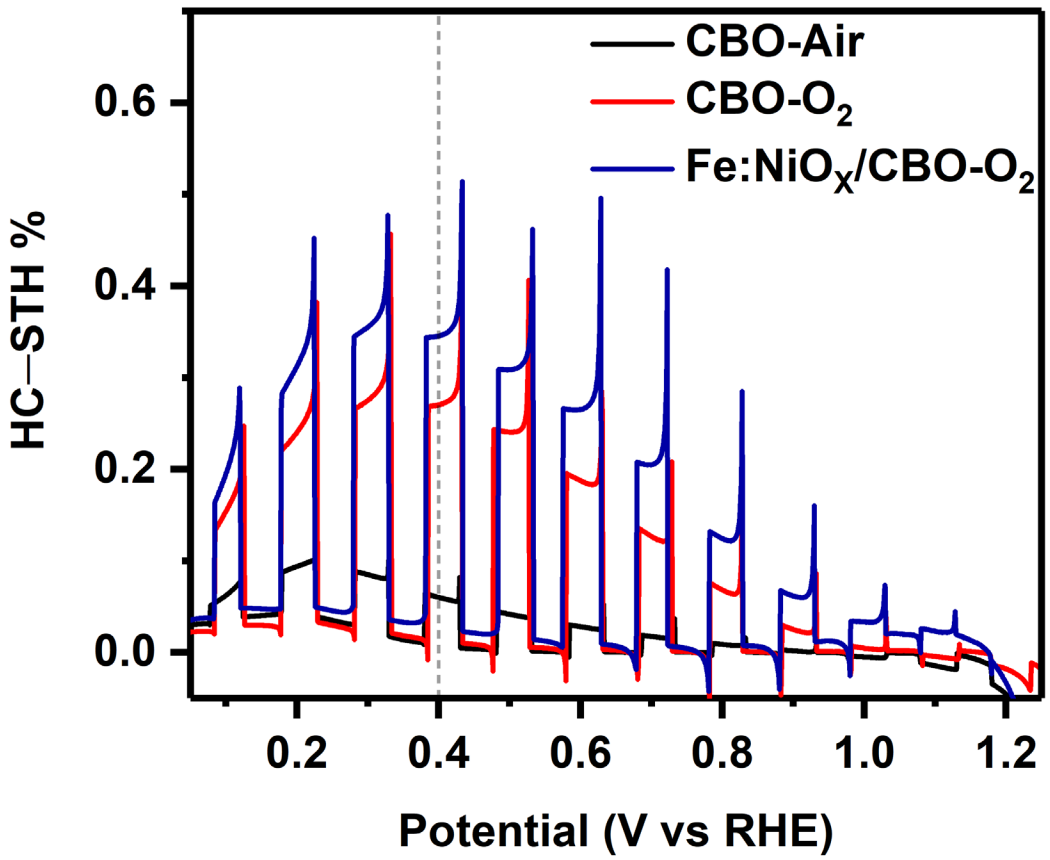

Figure S26. HC–STH efficiency calculations from LSV comparison curves with respect to applied potential for CBO-Air and CBO-O_2 photocathode with/without Fe:NiO_X hole transport layer in 0.5 M Na_2SO_4 (pH:6.6) electrolyte solution.

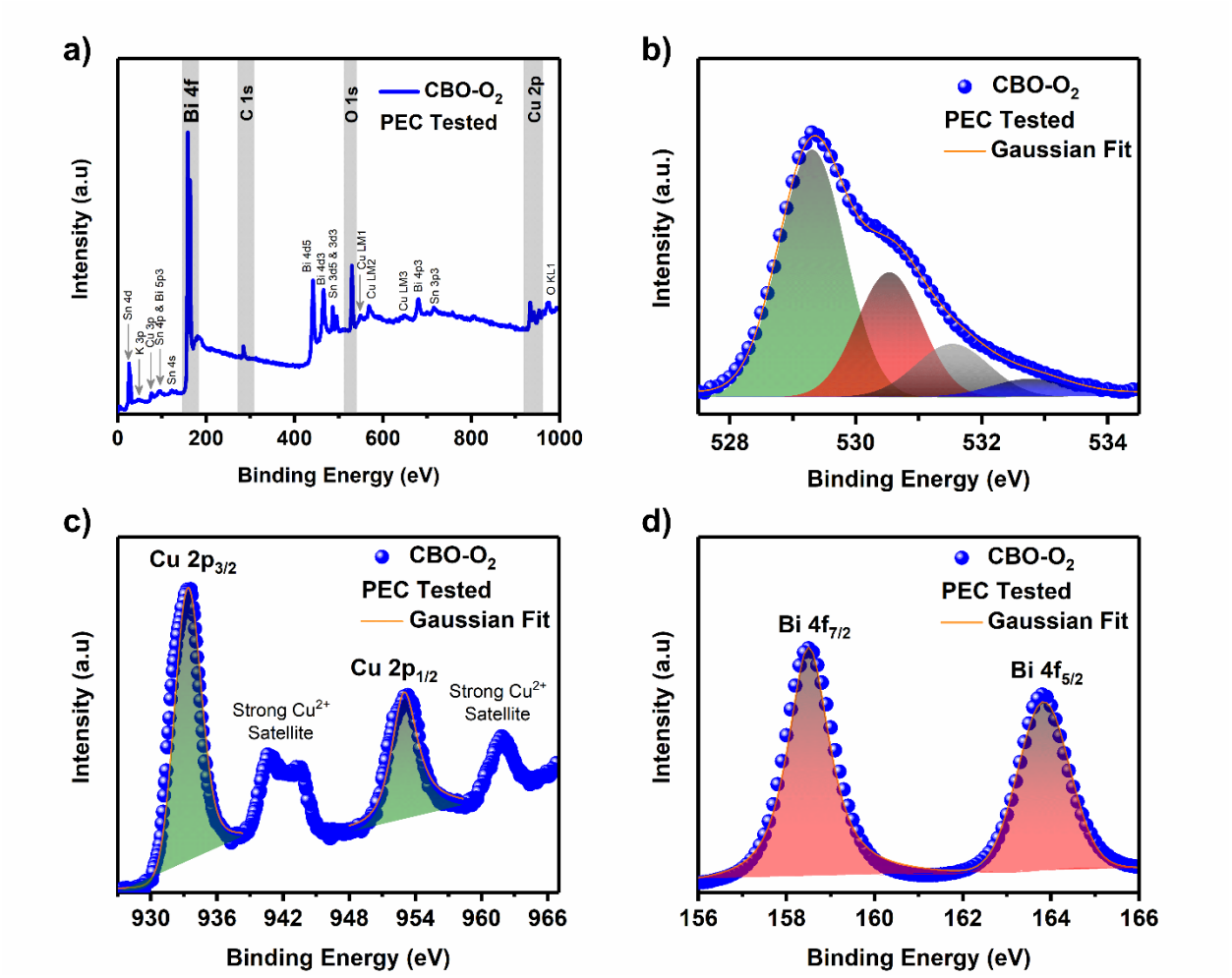

Figure S27. FTO/Fe:NiO_X/CBO-O_2 photocathode after PEC experiments tested (without scavenger). a) XPS survey spectrum and (b-d) deconvoluted XPS of O 1s, c) Cu 2p, and d) Bi 4f core-level spectrum.

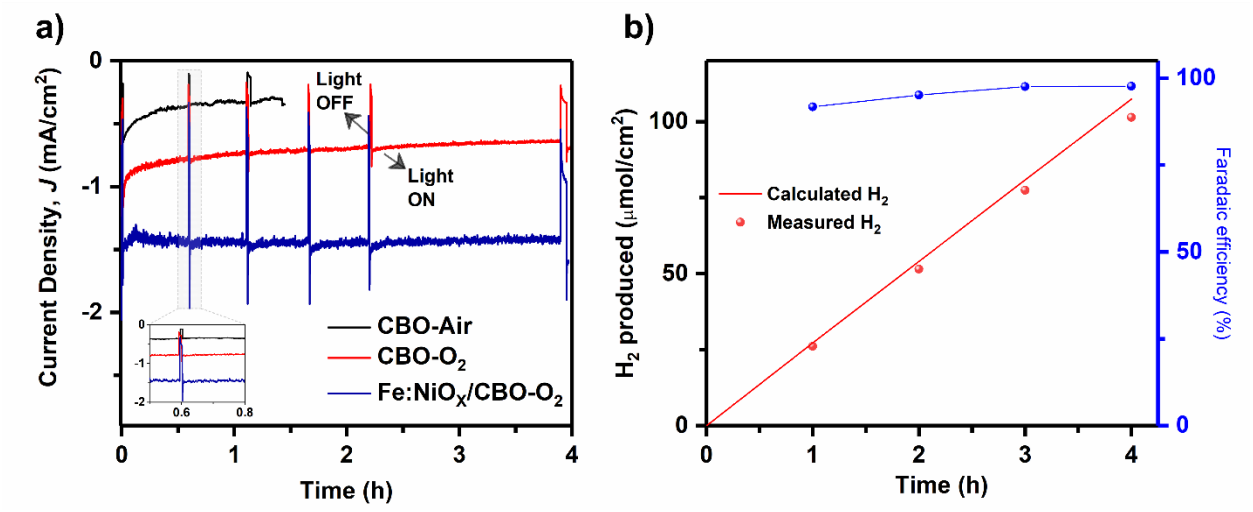

Figure S28. (a) Photocurrent density measurements for CBO photocathodes at 0.2 V_{RHE} in 0.5 M Na_2SO_4 aqueous solutions with respect to time. Inset show chopped light response at about 30 min. (b) Amount of hydrogen gas evolved under 1 sun light illumination with respect time using a Fe:NiO_X/CBO-O_2 with introduced protecting layer photocathode. The theoretical and experimental values represent the expected and observed amount of H_2 produced.

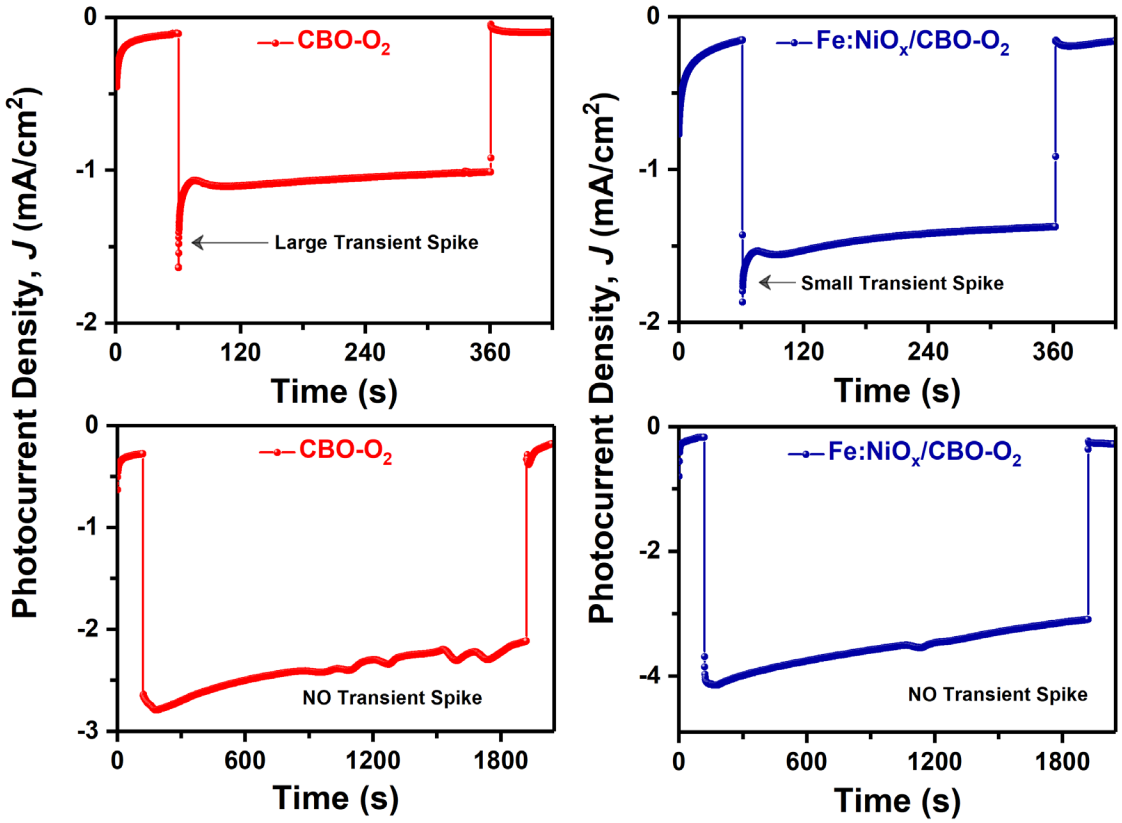

Figure S29. Transient photocurrent spike difference between 0.5 M Na_2SO_4 aqueous (top) with applied potential is 0.2 V_{RHE} and addition of 0.2 M $K_2S_2O_8$ electron scavenger (bottom) at 0.4 V_{RHE} applied potential.

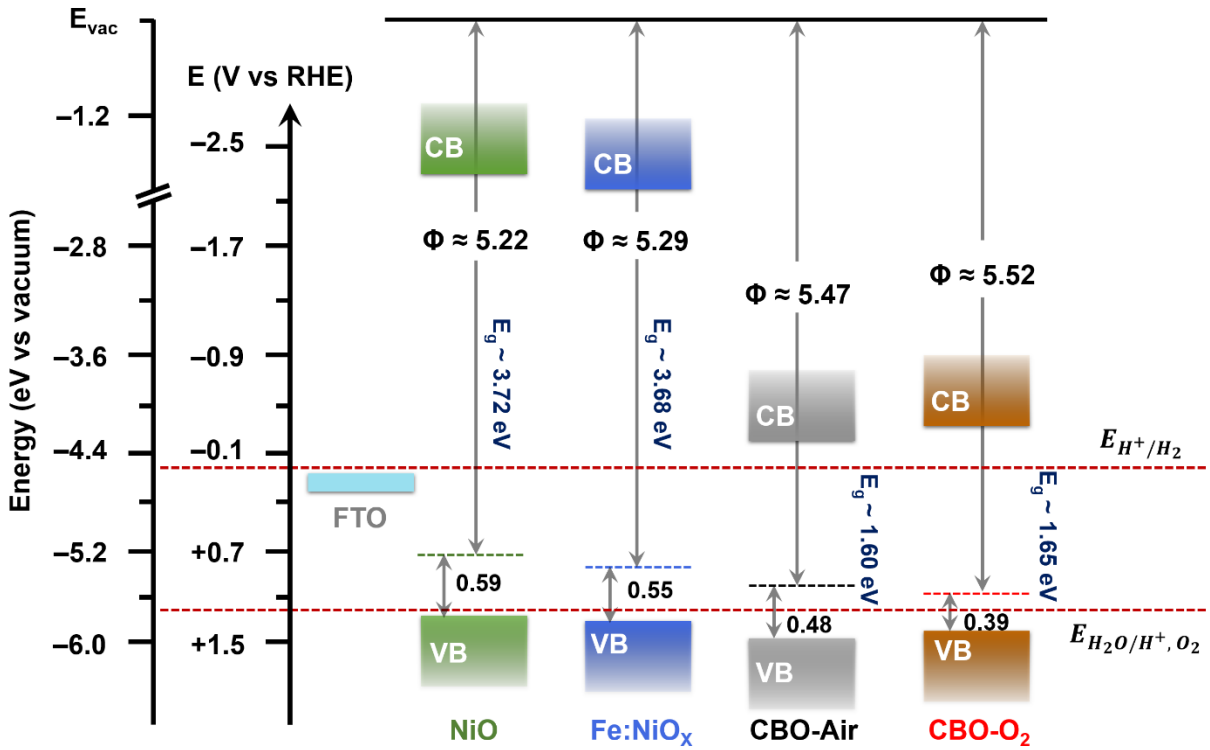

Figure S30. Schematic illustration of estimated energy band structure, composing of work functions, E_F, E_F-E_V, VBM, CBM, and band-gap in the vacuum energy level scale and potential vs. RHE scale, of the bare NiO, Fe-doped NiO_X HTLs, CBO-Air, and CBO-O_2 photoelectrodes deduced from the UPS and absorption data. For comparison, FTO flat-band potentials is included.

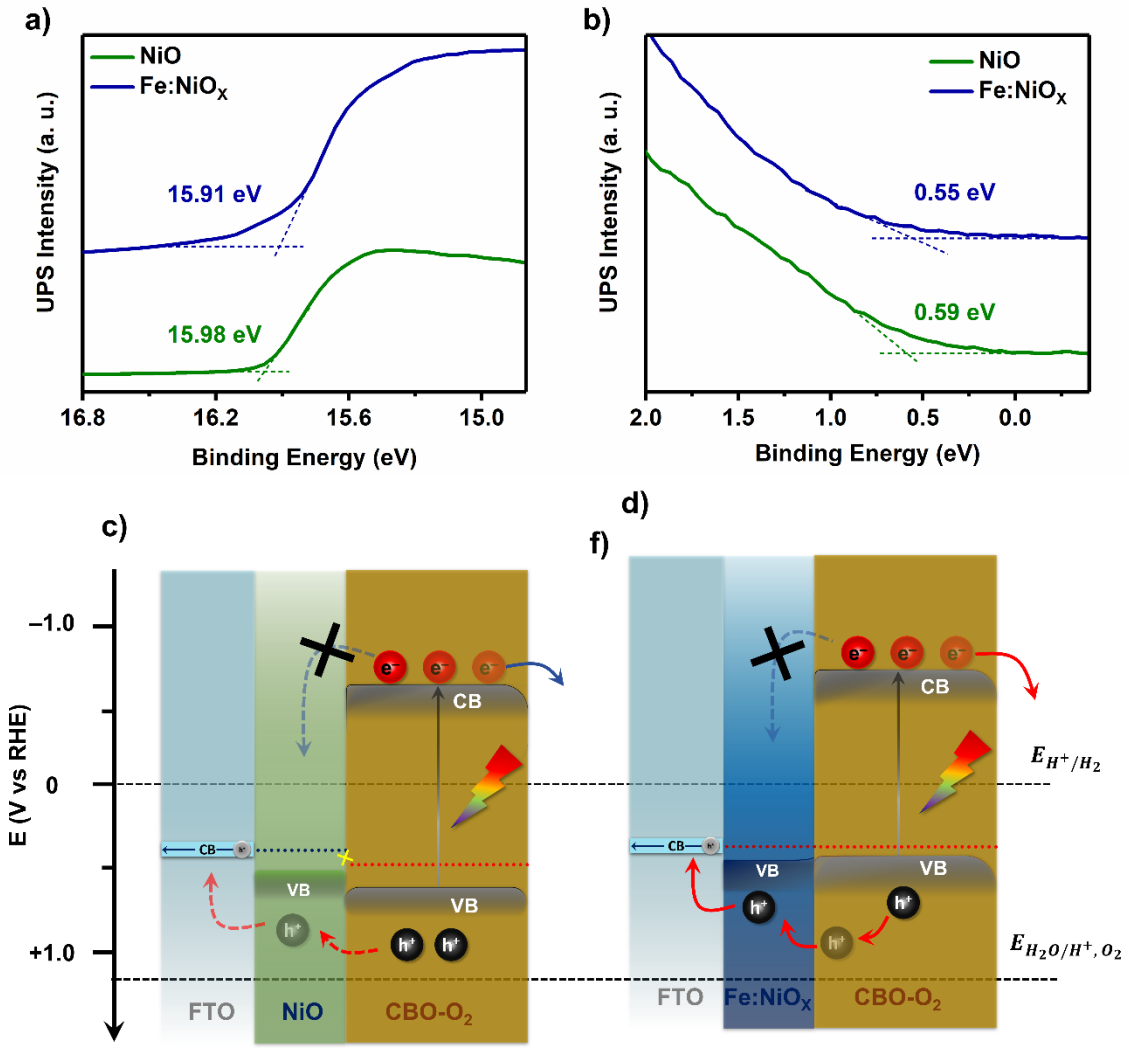

Figure S31. UPS curves for the bare NiO and Fe:NiO_X hole-transport layers: (a) E_{cutoff} and (b) E_{edge} obtained from the He–I radiation at 21.2 eV. (c) Schematic energy band diagram showing the difference between (c) bare NiO and (d) Fe-doped NiO_X HTL effect under the CBO-O_2 photocathode with respect to FTO after the equilibrium.

Table S1. Estimated flat band potentials and acceptor density for carrier-gas flow annealed CBO photoelectrodes measured under dark conditions with 0.5 M of Na_2SO_4 aqueous solutions.

CBO carrier gas ratio	Flat-band potential [φ_{FB}] V_{RHE}	Acceptor density [N_A] cm^{-3}
CBO-Air (Furnace)[a]	1.176	3.91×10^{18}
N/O~4[b]	1.180	4.03×10^{18}
N/O~2	1.189	8.90×10^{19}
N/O~1	1.194	2.12×10^{20}
CBO-O_2[c]	1.203	1.10×10^{21}

Considering approximately similar environment in [a]muffle furnace and [b]tube furnace. [c]working pressure recorded as 0.25 torr under continuous flow of pure O_2 during heat treatment.

Table S2. XPS O 1s deconvoluted peak position and proportion of resolved lattice oxygen (O^{2-}) bound to Cu^{2+} and Bi^{3+} components as well as Oxygen vacancies, in CBO films.

Electrode	Binding Energy (eV)		Relative Amount [at.%.]				
	Cu^{2+}	Bi^{3+}	Cu^{2+}	Bi^{3+}	V_O[a]	OH^-_{surf}[b]	Cu/Bi
Unannealed	529.3	530.4	87.6	8.0	2.8	1.6	11
Air without K^+	529.3	530.4	79.8	8.2	10.2	1.8	9.8
CBO-Air (Furnace)	529.3	530.5	68.5	20.4	8.2	3.0	3.4
N/O~4	529.3	530.5	70.5	20.8	7.3	1.4	3.4
N/O~2	529.4	530.5	70.0	22.9	6.2	1.0	3.1
N/O~1	529.4	530.5	67.8	26.8	4.6	0.8	2.5
CBO-O_2	529.4	530.5	65.0	29.8	4.5	0.7	2.2
CBO-O_2 (PEC tested)	529.4	530.5	62.6	28.4	6.3	2.8	2.2

[a]surface oxygen vacancies and [b] OH- and C-O groups adsorbed on the surface.

Table S3. Elemental analysis (atomic. %) of prepared CBO films surfaces obtained from XPS.

Electrode	Cu	Bi	O	K	C	Cu/Bi
Unannealed	11.4	15.7	43.9	5.5	23.6	0.7
Air without K^+	3.1	5.4	71.2	--	20.3	0.6
CBO-Air (Furnace)	11.5	13.4	50.8	--	24.3	0.9
N/O~4	11.5	13.7	53.7	--	21.1	0.8
N/O~2	10.9	14.3	53.2	--	21.6	0.8
N/O~1	9.8	14.4	53.3	--	22.5	0.7
CBO-O_2	9.0	15.1	54.2	--	21.7	0.6
CBO-O_2 (PEC tested)	9.3	15.3	53.2	--	22.2	0.6

Table S4. Atomic ratio percentage obtained from EDS mapping for Cu-to-Bi components in prepared CBO electrodes.

Element	CBO-Air	CBO-O_2
Cu	12.9	9.2
Bi	28.0	28.2
O	59.1	62.6

Table S5. Comparison of atomic ratio percentage obtained from XPS spectrum and EDS mapping for Cu-to-Bi components in prepared CBO-air and CBO-O_2 electrodes.

Electrode	XPS Atomic%			EDS Atomic%		
	Cu	Bi	Cu/Bi	Cu	Bi	Cu/Bi
CBO-Air	11.5	13.4	0.9	12.9	28.0	0.5
CBO-O_2	9.0	15.1	0.6	9.2	28.2	0.3

Table S6. Series (Rs) and charge-transfer (R_{ct}) resistance for the CBO-O_2 and Fe:NiO_X/CBO-O_2 photocathodes comparison with CBO-Air at 0.4 V_{RHE} in 0.5 M Na_2SO_4 (pH~ 6.6).

Photocathode	R_S (Ω·cm^2)	R_{ct} (Ω·cm^2)
CBO-Air	70.0	4606.2
CBO-O_2	55.0	3148.3
NiO/CBO-O_2	44.3	2751.0
Fe:NiO_X/CBO-O_2	26.8	612.8

Table S7. Summary of recent literature on CBO based photocathodes at required potential photocurrent density for water reduction in the neutral electrolyte solution. *The photocurrent values were roughly read from LSV curves in the corresponding literature.

Photocathode Structure	Preparation Method	Heat-Treatment	Electrolyte type	pH	Photocurrent Density at 0.2 V_{RHE} [$mA \cdot cm^{-2}$]	Ref.
CBO-O_2 Fe:NiO_X/CBO-O_2	Spin-coating/ Pulsed-Electrodeposition	450 ℃ at O_2 partial pressure (0.5 mBar)	0.5 M Na_2SO_4	6.6	–1.23 –1.56	This work
$CuBi_2O_4$	Drop-coating	550 ℃ in Air Heating	0.1 M Na_2SO_4	6.8	–0.46	[S1]
$CuBi_2O_4$/CuO	Chemical Bath and Doctor-blending	400 ℃ in Air Heating	0.1 M Na_2SO_4	6.8	–0.60	[S2]
$CuBi_2O_4$/CuO	Solution Combustion/ Spray-coating	Pre-heated 300 ℃/350 ℃ Air heating	0.1 M Na_2SO_4	6.8	–0.30	[S3]
CuO/$CuBi_2O_4$/Pt	Drop-coating	500 ℃ in Air Heating	0.3 M K_2SO_4 + 0.1 M PBS	6.8	–0.24	[S4]
Au/$CuBi_2O_4$/Pt	Electrodeposition	550 ℃ in Air Heating	0.1 M Na_2SO_4	6.8	–1.00	[S5]
$CuBi_2O_4$/ZnSe/TiO_2	Drop-coating	450 ℃ in Air Heating	0.3 M K_2SO_4 + 0.2 M PBS	6.65	–0.60	[S6]
$CuBi_2O_4$/Au/C	Drop-coating	450 ℃ in Air Heating	0.3 M K_2SO_4 + 0.2 M PBS	6.68	–0.52	[S7]

$CuBi_2O_4$/Polythiophene	Drop-coating	450 ℃ in Air Heating	0.3 M K_2SO_4 + 0.2 M PBS	6.66	–0.51	[S8]
$CuBi_2O_4$/$BiVO_4$	Electrodeposition	500 ℃ in Air Heating	0.1 M Na_2SO_4	6	–0.48	[S9]
$CuBi_2O_4$/rGO	Drop-coating/Spin-coating	450 ℃ in Air Heating	0.5 M Na_2SO_4	6.8	–0.25	[S10]
Ag-$CuBi_2O_4$/NGQD	Drop-coating	550 ℃ in Air Heating	0.5 M Na_2SO_4	6.6	–0.08	[S11]
O_V-$CuBi_2O_4$/Zn-$CuBi_2O_4$	Drop-coating	550 ℃ in Air Heating	0.3 M K_2SO_4 + 0.2 M PBS	6.65	–0.64	[S12]
CuO/$CuBi_2O_4$	Electrodeposition	450 ℃ in Air Heating	0.5 M Na_2SO_4	7	–0.80	[S13]
$CuBi_2O_4$/TiO_2	Electrodeposition/ Drop-casting	550 ℃ in Air (Bi_2O_3)/ 550 ℃ in O_2 (Cu^{2+}-Bi_2O_3) Heating	0.1 M Na_2SO_4	6.8	–0.90	[S14]
NiO/$CuBi_2O_4$	Mechanochemical-Pulsed Laser deposition	800 ℃ in Air/PLD in O_2 partial pressure	0.1 M PBS	8.55	–0.45 @ 0.4V_{RHE}	[S15]

*PBS represents phosphate buffer solution.

Table S8. Summary of recent literature on CBO based photocathodes at required potential photocurrent density for water reduction in the neutral electrolyte solution with electron scavenger. *The photocurrent values were roughly read from LSV curves in the corresponding literature.

Photocathode Structure	Preparation Method	Heat-Treatment	Electrolyte type	Electron Scavenger	pH	Photocurrent Density at 0.4 V_{RHE} [$mA \cdot cm^{-2}$]	Ref.
CBO-O_2 Fe:NiO_X/CBO-O_2	Spin-coating/Pulsed-Electrodeposition	450 °C at O_2 partial pressure	0.5 M Na_2SO_4	$K_2S_2O_8$	7	−2.89 −4.50	This work
NiO/$CuBi_2O_4$	Mechanochemical-Pulsed Laser deposition	800 °C in Air/PLD in O_2 partial pressure	0.1 M PBS	H_2O_2	8.55	−1.5	[S15]
$CuBi_2O_4$ (Bi:Cu=1.5)	Spin-coating	550 °C in Air Heating	0.1 M $KHCO_3$	$Na_2S_2O_8$	8.2	−1.21 @ 0.6 V_{RHE}	[S16]
$CuBi_2O_4$/$Cu_{1.5}TiO_z$	Co-sputtering	400 °C in Ar (86%) & O_2 (14%) Heating	0.1 M $KHCO_3$	$Na_2S_2O_8$	8.2	−1.4	[S17]
$CuBi_2O_4$	Spin-coating	450 °C in Air Heating	0.3 M K_2SO_4+0.2 M PBS	H_2O_2	6.65	−3.90	[S18]
Cu:NiO/$CuBi_2O_4$	Electron-beam evaporation/ Spray-pyrolysis	Pre-heated 450 °C in Air	0.3 M K_2SO_4+0.2 M PBS	H_2O_2	6.65	−4.40	[S19]
Gradient $CuBi_2O_4$/ CdS/TiO_2/Pt	Spray-pyrolysis	Pre-heated 450 °C in Air	0.3 M K_2SO_4+0.2 M PBS	H_2O_2	6.65	−3.7	[S20]

*PBS represents phosphate buffer solution.

References

[S1] J. Li, M. Griep, Y. Choi, D. Chu, Chem. Commun. 54 (2018) 3331–3334.

[S2] R. Patil, S. Kelkar, R. Naphade, S. Ogale, J. Mater. Chem. A 2 (2014) 3661–3668.

[S3] M.K. Hossain, G.F. Samu, K. Gandha, S. Santhanagopalan, J.P. Liu, C. Janáky, K. Rajeshwar, J. Phys. Chem. C 121 (2017) 8252–8261.

[S4] H.S. Park, C.-Y. Lee, E. Reisner, Phys. Chem. Chem. Phys. 16 (2014) 22462–22465.

[S5] D. Cao, N. Nasori, Z. Wang, Y. Mi, L. Wen, Y. Yang, S. Qu, Z. Wang, Y. Lei, J. Mater. Chem. A 4 (2016) 8995–9001.

[S6] S. Wei, N. Xu, F. Li, X. Long, Y. Hu, L. Gao, C. Wang, S. Li, J. Ma, J. Jin, ChemElectroChem 6 (2019) 3367–3374.

[S7] N. Xu, F. Li, L. Gao, H. Hu, Y. Hu, X. Long, J. Ma, J. Jin, ACS Sustain. Chem. Eng. 6 (2018) 7257–7264.

[S8] N. Xu, F. Li, L. Gao, H. Hu, Y. Hu, X. Long, J. Ma, J. Jin, Int. J. Hydrogen Energy 43 (2018) 2064–2072.

[S9] S. Liu, J. Zhou, Y. Lu, J. Su, Sol. Energy Mater. Sol. Cells 180 (2018) 123–129.

[S10] A.K. Shah, T.K. Sahu, A. Banik, D. Gogoi, N.R. Peela, M. Qureshi, Sustain. Energy Fuels 3 (2019) 1554–1561.

[S11] C. Ma, D.-K. Ma, W. Yu, W. Chen, S. Huang, Appl. Surf. Sci. 481 (2019) 661–668.

[S12] S. Wei, C. Wang, X. Long, T. Wang, P. Wang, M. Zhang, S. Li, J. Ma, J. Jin, L. Wu, Nanoscale 12 (2020) 15193–15200.

[S13] S. Pulipaka, N. Boni, G. Ummethala, P. Meduri, J. Catal. 387 (2020) 17–27.

[S14] Q. Zhang, B. Zhai, Z. Lin, X. Zhao, P. Diao, J. Phys. Chem. C 125 (2021) 1890–1901.

[S15] J. Lee, H. Yoon, S. Kim, S. Seo, J. Song, B.-U. Choi, S.Y. Choi, H. Park, S. Ryu, J. Oh, S. Lee, Chem. Commun. 55 (2019) 12447–12450.

[S16] Z. Zhang, S.A. Lindley, R. Dhall, K. Bustillo, W. Han, E. Xie, J.K. Cooper, ACS Appl. Energy Mater. 2 (2019) 4111–4117.

[S17] Z. Zhang, S.A. Lindley, D. Guevarra, K. Kan, A. Shinde, J.M. Gregoire, W. Han, E. Xie, J.A. Haber, J.K. Cooper, Adv. Funct. Mater. 30 (2020) 2000948.

[S18] Y. Xu, J. Jian, F. Li, W. Liu, L. Jia, H. Wang, J. Mater. Chem. A 7 (2019) 21997–22004.

[S19] A. Song, P. Plate, A. Chemseddine, F. Wang, F.F. Abdi, M. Wollgarten, R. van de Krol, S.P. Berglund, J. Mater. Chem. A 7 (2019) 9183–9194.

[S20] F. Wang, W. Septina, A. Chemseddine, F.F. Abdi, D. Friedrich, P. Bogdanoff, R. van de Krol, S.D. Tilley, S.P. Berglund, J. Am. Chem. Soc. 139 (2017) 15094–15103.